ISSN 1070-3632, Russian Journal of General Chemistry, 2008, Vol. 78, No. 5, pp. 1081–1092. © Pleiades Publishing, Ltd., 2008.
Original Russian Text © M.N. Rumyantseva, V.V. Kovalenko, A.M. Gas'kov, T. Pagnier, 2008, published in Rossiiskii Khimicheskii Zhurnal, 2007, Vol. 51, No. 6, pp. 61–70.

Metal-Oxide Based Nanocomposites as Materials for Gas Sensors

M. N. Rumyantseva[a], V. V. Kovalenko[a], A. M. Gas'kov[a], and T. Pagnier[b]

[a] *Faculty of Chemistry, Moscow State University, Vorob'evy gory 1, Moscow, 119992 Russia*
[b] *Institut National Polytechnique de Grenoble, Grenoble, France*

Received September 10, 2007

Abstract—Correlations between the composition, structure, and sensor properties of SnO_2–$M^{II}O$ ($M^{II}O$ = Fe_2O_3, MoO_3, V_2O_5) nanocomposites prepared by wet chemistry synthesis were elucidated. The elemental and phase compositions of the materials, distribution of components between the bulk and surface, particle size, and specific surface area were examined. Surface modification of semiconductor oxides allows controlling the type and density of surface acid centers and redox properties of materials. The result is an increase in the sensor selectivity.

DOI: 10.1134/S1070363208050411

INTRODUCTION

The gas sensitivity of semiconductors is underlain by reversible effects resulting from chemisorption of molecules, formation of space charge areas, and variation of the concentration of the charge carriers in the subsurface layer. The size of the change of electric conductivity (sensor signal) is largely determined by the structural type of the semiconductor, the nature and concentration of surface reactive centers, and the real structure of the material: the size, structure, and degree of agglomeration of crystallites, specific surface area, and pore geometry. An essential drawback suffered by semiconductor sensors is low selectivity of the contribution made by this type of molecules in the gas phase to the total electric response. Therefore, materials for semiconductor sensors are studied mainly with the focus on increasing their selectivity.

Among the recently studied materials for active elements of gas sensors [1–3], the most extensive application is found by wide band gap semiconductor metal oxides: SnO_2, ZnO, In_2O_3, and WO_3. The unique features of these materials are determined by a favorable combination of their physical and chemical properties. The electric conductivity of oxide semiconductors is extremely sensitive to the composition of the surface, which reversibly varies as a consequence of surface reactions involving chemisorbed oxygen (O_2^-, O^{2-}, O^-) and the gas mixture components, proceeding at 100–500°C. The advantages offered by wide band gap semiconductor oxides include their stability in air, relative inexpensiveness, and easy preparation in the ultradispersed state.

The selectivity of wide band gap semiconductor oxides is improved by surface modification via creating complex inhomogeneous systems, M^IO–$M^{II}O$ nanocomposites, through introduction into a highly-dispersed oxide matrix of catalytic additions: platinum group metals Pt, Pd, Ru, Rh, or oxide catalysts, Fe_2O_3, La_2O_3, Cr_2O_3, Co_3O_4, V_2O_5, NiO, CuO, MoO_3, CeO_2. A developed surface of ultradispersed oxide semiconductors and poor solubility in them of catalytic additions suggests predominantly surface distribution of the modifiers.

Generally, surface modification implies not only changing the composition and size of nanocrystallites of semiconductor oxides, but also taking advantage of some additional options, among which the most important are the following:

– choosing a modifier that exhibits a catalytic activity in the solid–gas interaction examined;

– changing the reactivity of the material via changing the modifier concentration, i.e., via cluster–cluster interaction;

– choosing a "cluster–matrix" pair; the nature of the semiconductor oxide can affect the configuration of d

Table 1. Selection criteria for modifier in selective sensor of the gas tested

Gases tested	Modifying component of the nanocomposite
Reducing gases	
CO, H_2, CH_4	Noble metal dopant additions: Pt, Pd, Ru, Rh, Au
Lewis bases: NH_3	Metal oxides more acidic than SnO_2: V_2O_5, MoO_3, WO_3
Complex molecules with different functional groups	Metal oxides more basic than SnO_2: Fe_2O_3, In_2O_3, La_2O_3
Oxidizing gases	
O_2, O_3, NO_2	Electron donor additions – Sb_2O_5 Noble metal additions: Pt, Pd, Ru, Rh, Au

electrons of surface-localized transition metals and change the surface activity.

There were attempts to use electronegativity, electron affinity, thermodynamic characteristics of adsorption, work function, etc. as correlation parameters in directed search of dopants for sensor materials [4, 5]. However, in our opinion, the most promising catalytic approaches are those based on the "collective" and "local" site concept. The "collective" site approach is underlain by the chemisorption theory advanced by F. Vol'kenshtein [6]. It provides an idea of how the adsorbate affects the overall band structure of the modified matrix. This theory correlates the catalytic activity of the modifier directly to the valence state of the dopants in the oxide matrix and their influence on the charge carrier concentration in the semiconductor.

On the other hand, the "local" sites approach is underlain by the concept of a nonuniform surface, which treats interaction of a semiconductor oxide with the gas phase in terms of formation of surface complexes. In this case, the chemical nature of the modifier and its reactivity in acid–base or redox reactions plays the deciding role. Preliminary selection of the modifier can be based on analysis of the properties exhibited by the molecules of the tested gas and a large body of experimental data on heterogeneous catalysis for platinum group metals and metal oxides (Table 1) [7–9]. Clearly, the relationships established for catalysts are not necessarily valid in the case of sensor materials and should be verified experimentally.

We summarize here the results of studies into relationships among the composition, structure, and sensor properties of SnO_2–$M^{II}O$ ($M^{II}O$ = Fe_2O_3, MoO_3, V_2O_5) nanocomposites.

EXPERIMENTAL

Nanocrystalline SnO_2 and SnO_2–$M^{II}O$ ($M^{II}O$ = Fe_2O_3, MoO_3, V_2O_5) nanocomposites were prepared by various methods of chemical precipitation from solution [10–16].

The SnO_2-based nanocomposites were synthesized by thermal decomposition of α-stannic acid gel, followed by impregnation with salts of the corresponding metals. The α-stannic acid gel was precipitated from a $SnCl_4 \cdot 5H_2O$ solution with an ammonia solution (pH = 6.5–7.0) under permanent stirring at 0°C. The precipitate was separated by centrifugation, thoroughly washed with distilled water to remove chloride ions till no reaction with Ag^+ took place, and dried at 100°C for one day. Next, the powder was impregnated with $Fe(NO_3)_3$, $(NH_4)_6 \cdot Mo_7O_{24}$, or VO_2NO_3 solutions, dried at 100°C, and annealed in air at 300, 500, or 700°C for one day. The $M^{II}O$-based nanocomposites were prepared by coprecipitation of α-stannic acid and hydroxides of the corresponding metals, followed by heat treatment.

The nanocomposites were characterized by a number of physicochemical methods; their elemental and phase compositions were determined, as well as the distribution of the components between the bulk and surface of the crystalline grains, the particle size, and specific surface area.

The elemental composition of the nanocomposites was examined by local X-ray spectral analysis (LXSA). Quantitative analysis was carried out using a Jeol 840A microscope with a PGT microanalysis system. Mechanical mixtures of the oxides served as references. The analysis was carried out for three 50×50-μm^2 windows at the accelerating voltage of 20 keV. The composition of the samples was calculated as the ratio of the concentrations of the cations:

$$x = \frac{[M^{II}]}{[M^{II}] + [Sn]}. \quad (1)$$

The X-ray diffraction spectra of the nanocomposites were obtained at the European Synchrotron Radiation Facility (ESRF, Grenoble) with the use of monochromatic radiation at λ_{synchr} = 0.72004 Å. The size of the coherent scattering areas (CSAs) was estimated from the broadening of the reflections in the X-ray diffraction spectra by the Scherer formula:

$$d = \frac{k\lambda}{\beta\cos\theta}, \quad (2)$$

where d is the average CSA size; β, half-width of the diffraction peak; λ, radiation wavelength; θ, diffraction angle; and k = 0.9.

The transmission electron-microscopic and local electron diffraction examinations of the samples were carried out on a Phillips CM30 SuperTwin electron microscope with the resolution of 0.19 nm (Dr. J. Arbiol, the University of Barcelona, Spain).

The Mössbauer spectra were measured on an electrodynamic spectrometer in the permanent acceleration mode using $Ca^{119m}SnO_3$ and $^{57}Co(Rh)$ sources at room temperature. The isomer shifts are given relative to $CaSnO_3$ or α-Fe at 295 K.

To examine the sensor properties, the substances of interest were applied as a paste to a chip with platinum junctions and a platinum meander as the heater on an Al_2O_3 substrate. The conductivity was measured at the direct current in air containing 500 ppm NH_3 at 400°C, as well as upon introduction of 1 μl of ethanol into an air stream at 275°C. The sensor signal S was estimated from the conductivity in air G_{air} and in the gas tested G_g by the formula:

$$S = \frac{G_g - G_{air}}{G_{air}}. \quad (3)$$

RESULTS AND DISCUSSION

Mutual Distribution of the Components

The distribution of the second component between the bulk and surface of the crystalline grains of the major phase is of extreme importance for the functional properties of nanocomposites. Introduction of a dopant into the crystal structure of the semiconductor oxide is responsible for formation of impurity levels, the effect of balancing the donor oxygen vacancies by acceptor impurity defects, and modulation of the band relief of the semiconductor [12]. Segregation of the second oxide component can result in formation of *p–n* junctions in the intergrain contact area, which will inevitably affect the electrophysical properties of the material. Also, the distribution of the catalyst between the bulk and surface of the crystalline grains governs its performance in reactions with the gas phase. Taken together, these factors significantly affect the sensor properties of nanocomposites.

The intrinsic phase of the second component in nanocomposites is often detected only at fairly large x values and high annealing temperatures. This makes elucidation of the mutual distribution of the components a difficult task. When the second component phase is not detected, this can be associated with formation of a solid solution and/or segregation of M^{II} on the surface of the crystallites of the major component. The contributions from either factor is determined both by fundamental reasons, e.g., the difference in the ionic radii between Sn^{4+} (0.69 Å) and M^{n+} [17], and the synthesis conditions, the M^{II} content and the annealing temperature. Based on the ionic radii of the metal cations in the octahedral surrounding, SnO_2-based solid solutions can be presumably formed upon introduction of Ni^{2+} (0.70 Å), Fe^{3+} (0.645 Å), and Mo^{4+} (0.65 Å), though are hardly probable in the case of Cu^{2+} (0.73 Å), Zn^{2+} (0.745 Å), La^{3+} (1.06 Å), Ce^{4+} (0.80 Å), and V^{5+} (0.54 Å).

Formation of a solid solution is suggested unambiguously by variation of the crystal lattice parameters of the major component phase with increasing x. However, precise determination of the parameters from the X-ray diffraction patterns of nanocrystalline systems is often complicated by substantial broadening of the reflections. In this situation, valuable additional information on the mutual distribution of the components in nanocomposites can be derived from transmission electron-microscopic, electron diffraction, Raman spectroscopic, and Mössbauer spectroscopic data.

SnO_2–Fe_2O_3 Nanocomposites

According to the X-ray diffraction data, in SnO_2–Fe_2O_3 nanocomposites obtained by impregnation and coprecipitation of hydroxides, a two-phase area corresponds to the composition range $0.09 \le x \le 0.52$ at 300°C and $0.09 \le x \le 0.85$ at 500 and 700°C [13].

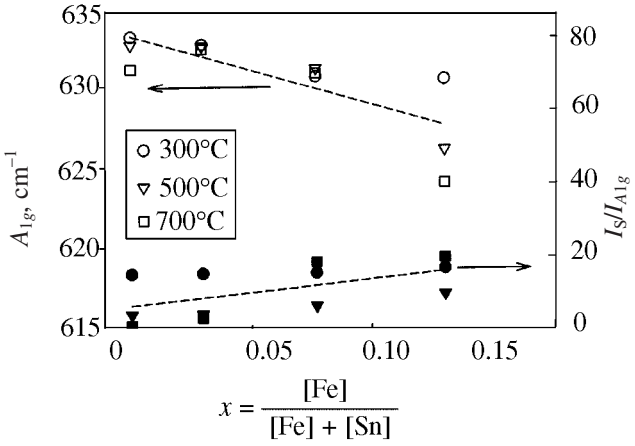

Fig. 1. Peak position of the A_{1g} line of SnO_2 and I_S/I_{A1g} ratio: (I_S) integrated intensity of the surface modes and (A_{1g}) integrated intensity of the A_{1g} line.

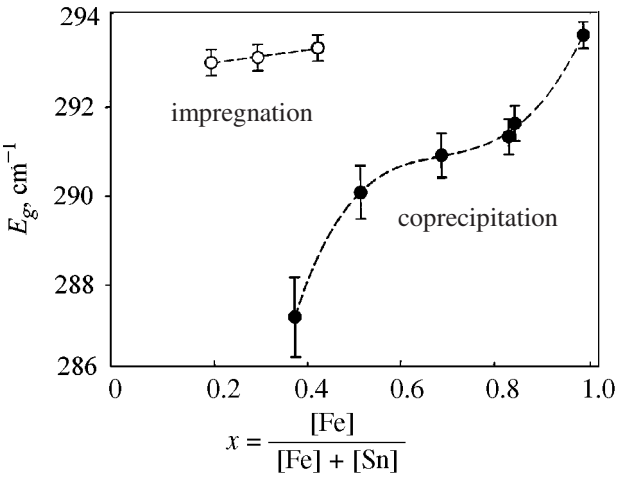

Fig. 2. Peak position of the E_g line of Fe_2O_3 in the Raman spectra of the SnO_2–Fe_2O_3 nanocomposites prepared by the impregnation and coprecipitation methods.

The observed variation of the unit cell parameters *a* and *c* of SnO_2 and Fe_2O_3 for this system suggests formation of cassiterite- and hematite-based solid solutions. In all the cases examined, the change of the crystal lattice parameters is determined by the elemental composition of the nanocomposite and the annealing temperature. The unit cell parameters of neat SnO_2 do not change with increasing annealing temperature; hence, the parameters *a* and *c* are associated with formation of cassiterite-based solid solutions in the SnO_2–Fe_2O_3 system. The unit cell parameters *a* and *c* of SnO_2 tend to decrease at $0 \le x \le 0.31$. The solubility of Fe in SnO_2 tends to decrease with increasing annealing temperature. With increasing Sn content in the nanocomposites, the unit cell parameters *a* and *c* of α-Fe_2O_3 tend to increase, more profoundly at low annealing temperatures of 300 and 500°C. The trends in variation of these parameters are consistent with those for the ratio of the ionic radii of Sn^{4+} (0.69 Å) and Fe^{3+} (0.645 Å). The content of the second component in a solid solution (Fe in SnO_2 and Sn in Fe_2O_3) cannot be determined directly by LXSA because of a small particles size in the nanocrystalline systems. The change in the unit cell parameters of SnO_2 and Fe_2O_3 suggests that the solubility of Fe in SnO_2 and Sn in Fe_2O_3 is much lower than the total content of the corresponding element as determined by LXSA. The solubility of Sn in α-Fe_2O_3 for single crystalline samples does not exceed 1 at.% [18].

The second component not incorporated into a solid solution can either form crystallites of its intrinsic phase or segregate into a two-dimensional layer which is not detected by X-ray diffraction method. Because of distinctions in the crystal structures of SnO_2 and α-Fe_2O_3 and the need in the charge balancing in the case of heterovalent substitution, there can be no very wide ranges of existence of solid solutions. A higher defectiveness of the matrix in the nanocomposites in the case of low-temperature annealing is responsible for enhanced solubility of the second component. A decrease in the solubility of Fe in SnO_2 and Sn in Fe_2O_3 with increasing annealing temperature was demonstrated earlier by EXAFS and Mössbauer spectroscopic examinations [19].

Additional information about the mutual distribution of the components in SnO_2–Fe_2O_3 ($0 \le x \le 0.13$) nanocomposites obtained by impregnation can be derived from the Raman spectra (Fig. 1). The main A_{1g} line of SnO_2 shifts to smaller wavenumbers with increasing x, thereby validating formation of a SnO_2-based solid solution.

Also, valuable information is provided by the parameter

$$I_r = \frac{I_S}{I_{A1g}}, \quad (4)$$

where I_S is the integrated intensity of the surface modes of nanocrystalline SnO_2 [20], and I_{A1g}, integrated intensity of the A_{1g} line in the Raman spectrum.

Boulova et al. [21] used this parameter to illustrate the possibility of formation of a CuO monolayer on the SnO_2 grain surface in the SnO_2–CuO nanocomposites. In the SnO_2–Fe_2O_3 system, an increase in I_r with increasing x suggests that there is no specific interaction between SnO_2 and α-Fe_2O_3 on the crystallite surface. Thus, Fe atoms that were not incorporated into a solid solution form three-dimensional α-Fe_2O_3 particles, rather than an oxide monolayer, like in the case of SnO_2–CuO. These three-dimensional particles can be detected only by Raman spectroscopy which is more sensitive to Fe_2O_3 than X-ray diffraction.

Importantly, for the samples obtained by decomposition of hydroxides, the Raman spectrum of hematite smoothly changes upon addition of tin, and the degree of crystallinity of α-Fe_2O_3 decreases. The samples obtained by impregnation of $SnO_2 \cdot nH_2O$ gel exhibit a sudden change from the nanocrystalline SnO_2 (x = 0.08) to a well-crystallized α-Fe_2O_3 (x = 0.18) phase. Analysis of the Raman spectral characteristics, the peak position and the width of the most intense line of hematite (E_g), reveals distinctions in the distributions of the components for nanocomposites prepared by different methods (Fig. 2). The parameters of the E_g line of Fe_2O_3 in the spectra of the nanocomposites obtained by impregnation are close to those corresponding to the α-Fe_2O_3 phase. In the Raman spectra of the coprecipitated samples, by contrast, the wavenumber corresponding to the E_g maximum of Fe_2O_3 monotonically increases, and the line width monotonically decreases with increasing x. Such spectral changes suggest formation of crystallites of the α-Fe_2O_3 phase in the samples obtained by impregnation and of an α-Fe_2O_3-based solid solution in the coprecipitated samples. In the former case, the $Fe(NO_3)_3$ precursor is spread over the surface of the disperse matrix of the dried α-stannic acid gel, and upon heat treatment, when the solubility of Fe(III) is exceeded, the excess of this component is crystallized in the cassiterite structure as an individual oxide phase. In the case of coprecipitation of hydroxides, the tin and iron atoms in the precursor occur in each other's nearest surrounding, and cassiterite- and hematite-based solid solutions are formed.

Details on the mutual distribution of the components in the SnO_2–Fe_2O_3 nanocrystalline system can be derived from the Mössbauer spectra measured with the use of two Mössbauer isotopes, ^{57}Fe and ^{119}Sn. The system of interest contains one magnetically ordered component (α-Fe_2O_3 is an antiferromagnetic with T_N = 960 K); hence, the ^{57}Fe spectra allow elucidating the size distribution pattern for the α-Fe_2O_3 crystallites [22]. Another essential advantage is offered by spin polarization of nonmagnetic tin ions, created by the neighbor 3d cations, which is responsible for magnetic hyperfine splitting in the spectra of ^{119}Sn, characterizing the tin distribution with respect to the magnetically ordered α-Fe_2O_3 crystallites [18]. For the first time, the parameters of the magnetic hyperfine splitting structure of ^{119}Sn were determined for a samples with minor, up to 0.5 at %, additions of Sn^{4+} ions in the bulk of the α-Fe_2O_3 crystalline particles [18, 23, 24]. It was shown that the Sn^{4+} ions occupy sites of the same kind with the characteristic magnetic hyperfine field H(Sn) = 123 kOe and the isomer shift δ = +0.15 mm s^{-1} at 295 K. These parameters allowed identification of the Sn^{4+} ions in the structure of the matrix examined. We found that the maximal content of Sn^{4+} in α-Fe_2O_3 does not exceed 1 at % for co-precipitated samples after annealing at 900°C [18]. Further examination of the Sn/Fe = 1:1 composite prepared in a similar way showed that the α-Fe_2O_3 crystallites exhibit superparamagnetic properties, which suggests their small size (d < 14 nm) [25].

The ^{119}Sn spectra of the SnO_2–Fe_2O_3 samples with a low iron content ($x \le 0.09$) are represented by a singlet with the parameters of neat SnO_2. In the ^{57}Fe spectrum (297 K), no magnetic hyperfine structure is observed; there is a quadruple doublet with δ ~0.3 mm s^{-1} and Δ ~1 mm s^{-1}. The ^{57}Fe parameters suggest a fairly uniform distribution of Fe_2O_3 in the SnO_2 sample without formation of α-Fe_2O_3 clusters over 10 nm in size, which is typical for a cassiterite-based solid solution.

Examination of the nanocomposites with a high iron content, $0.84 \le x \le 1$, allowed estimating the solubility of Sn(IV) in hematite. The ^{119}Sn spectrum (80 K) of the nanocomposite with x = 0.84 revealed an unexpectedly high content of the Sn^{4+} cations with spin polarization. This suggests that, in this sample, over 2/3 of tin atoms have iron cations in their local surrounding. Annealing at 900°C destroys this structure, and a SnO_2 phase is formed. A similar, though much less prominent, process is observed for the SnO_2–Fe_2O_3 (x = 0.995) nanocomposite: Upon annealing at 900°C, an additional minor contribution from the nonmagnetic component is observed in the middle part of the spectrum. No SnO_2 segregations were revealed for annealing of the nanocomposite with

the minimal tin content (x = 0.998). With increasing annealing temperature to 900°C the parameters of the ^{119}Sn spectrum remain unchanged and correspond to those obtained earlier for a Sn(IV)–α-Fe_2O_3 substitution solid solution [18, 24, 26–29]. Thus, the apparent solubility of Sn(IV) in hematite decreases with increasing annealing temperature, and at 900°C it does not exceed 0.3–0.4 at % Sn.

The ^{57}Fe spectra (297 K) of the nanocomposite (x = 0.84) annealed at 300 and 500°C [19] are superpositions of a sextet with the parameters of α-Fe_2O_3 and a central doublet which can be assigned to small (superparamagnetic) α-Fe_2O_3 particles up to 14 nm in diameter [22]. At 80 K, the ^{57}Fe spectra contain only a sextet corresponding to a magnetic hyperfine structure with the parameters $\delta = 0.48 \pm 0.05$ mm s^{-1}, $H = 525 \pm 10$ kOe. This suggests that the samples do not contain α-Fe_2O_3 crystallites less than 8 nm in size [22]. The ^{57}Fe spectrum (297 K) of the SnO_2–Fe_2O_3 nano-composite (x = 0.84) annealed at 700°C exhibits a magnetic hyperfine structure only, which suggests crystallization of superparamagnetic α-Fe_2O_3 particles with the diameter $8 < d < 14$ nm.

Comparison with the data obtained using ^{57}Fe and ^{119}Sn probe ions at 80 K allows a conclusion that approximately two thirds of the tin atoms are spin-polarized atoms, with the remaining one third occurring as nonmagnetic clusters of the SnO_2 type, while 100% iron occurs in a magnetically ordered state. This is indicative of partial segregation of tin around the smallest α-Fe_2O_3 crystallites. Indeed, a larger specific surface area of the particles coated with tin ($8 < d < 14$ nm) provides explanation to the presence of spin-polarized Sn^{4+} ions whose amount is much greater than the maximal tin concentration in the crystallite bulk. Also, the fact that tin occupies sites with nonequivalent cation (magnetic) surrounding on the α-Fe_2O_3 crystallite surface explains the lack of a resolved structure in the magnetically split component.

Presumably, different Fe^{3+}–O–Sn^{4+} exchange couplings were yielded by decomposition of the corresponding hydroxides. Tin segregation on the α-Fe_2O_3 crystallite surface should prevent their further growth. Annealing at 700°C completely destroys the Fe^{3+}–O–Sn^{4+} exchange couplings. This is consistent with a poor solubility of Sn^{4+} in the α-Fe_2O_3 bulk, which results in rapid saturation of the subsurface layers and segregation of SnO_2 clusters with further growth in size of small crystallites.

SnO_2–V_2O_5 Nanocomposites

In SnO_2–V_2O_5 nanocomposites, the two-phase area at 500°C corresponds to the composition range $0.27 < x \leq 0.90$ [16]. In the single-phase area at $x \leq 0.27$ the unit cell parameters of SnO_2 decrease, owing most likely to formation of a solid solution of V(V) in tin dioxide (the ionic radii of Sn^{4+} and V^{5+} are 0.69 and 0.63 Å, respectively). The maximal solubility of V(V) was estimated from the decrease in the unit cell volume according to Vegard's law at ~3 at %. In the composition range $0.90 \leq x < 1$, the unit cell parameters of V_2O_5 do not change because of a poor solubility of Sn(IV) in V_2O_5 due to a strong difference in the ionic radii of Sn^{4+} and V^{5+}.

Additional information on the mutual distribution of the components in SnO_2–V_2O_5 ($0.5 \leq x \leq 1$) nanocomposites was derived from scanning electron-microscopic images recorded in the chemical contrast mode on an LEO S440 instrument. Figure 3 presents a SEM image of the SnO_2–V_2O_5 (x = 0.90) nanocomposite. The sample contains irregularly shaped particles, from 30 to 300 nm in size. In the chemical contrast mode, against a uniform background, there are scarce lighter areas, under 10 nm in size. This suggests tin segregation and the presence of individual SnO_2 nanocrystallites on the surface and in the bulk of the V_2O_5 phase grains. Comparison of the results of examination of SnO_2–V_2O_5 ($0.5 \leq x \leq 1$) nanocomposites by X-ray diffraction and scanning electron microscopy methods suggests absorption of the tin dioxide particles by the V_2O_5 phase during crystallization.

SnO_2–MoO_3 Nanocomposites

In SnO_2–MoO_3 nanocomposites, the two-phase area at 500°C corresponds to the $0.04 < x \leq 0.75$ composition range [14, 30]. The strongly broadened reflections of the tin dioxide phase and superposition of the lines of SnO_2 and MoO_3 prevent calculation of the crystal lattice parameters with an accuracy sufficient for postulating the existence of solid solutions.

A high-resolution transmission microscopic examination revealed in nanocomposites with a low Mo content ($x \leq 0.1$) a change in the interplanar spacings, as well as a minor change in the unit cell parameter of SnO_2, which is enhanced with increasing x [30]. This suggests the presence of Mo in the crystal structure of SnO_2 and formation of a solid solution. With further increase of x, at $x > 0.1$, the crystal structure of SnO_2 is

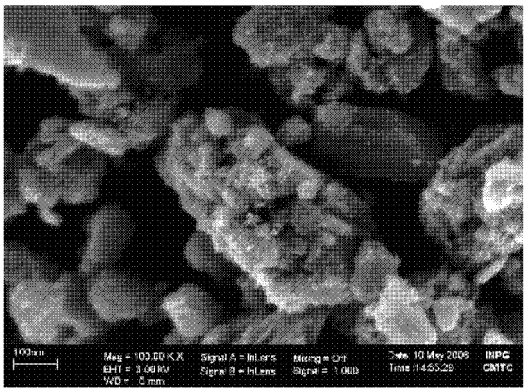

Fig. 3. SEM images of SnO_2–V_2O_5 ($x = 0.90$) nanocomposite.

stabilized. At $x = 0.04$, the β-MoO_3 phase is formed on the surface of the tin dioxide particles as segregation. At $x > 0.17$, the β-MoO_3 phase is converted to large (> 100 nm) α-MoO_3 particles whose surface contains small (3-nm) SnO_2 particles (Fig. 4).

A Raman spectroscopic examination also proved formation of monoclinic β-MoO_3 phase. The lines corresponding to β-MoO_3 are observed in the Raman spectrum of the SnO_2–MoO_3 nanocomposites in the $0.04 \le x \le 0.17$ range. In parallel, the A$I1g line of SnO_2 (634 cm^{-1}) decreases in intensity. A signal from α-MoO_3 is observed at $x = 0.15$. An increase in the molybdenum content to $x = 0.27$ results in complete disappearance of lines from β-MoO_3. The presence of β-MoO_3 phase in the nanocomposites annealed at 500° C was unexpected, since the β-MoO_3→α-MoO_3 phase transition in three-dimensional samples occurs below 400°C [31]. Probably, the β-MoO_3 phase is stabilized on the surface of small (~3-nm) tin dioxide particles.

Examination of the mutual distribution of the components in the SnO_2–MoO_3 nanocomposites was supplemented by analysis of the absorption near edge fine structure of the electron energy loss K spectra [30]. The analysis was carried out separately for SnO_2 and MoO_3 crystallites. The spectrum of SnO_2 contains two lines, S_1 and S_2, at 535 and 542 eV, respectively. The MoO_3 particles in the same spectral region also exhibit two lines, a major peak M_1 (535 eV) with a pronounced shoulder M_2 (538 eV). The spectrum of the SnO_2 particles is governed by the O 2*p* electronic levels or hybridized O 2*p*–Sn 5*p* orbitals and corresponds to the tetrahedral surrounding in the first coordination sphere of oxygen in the cassiterite structure [32, 33]. The spectrum of the MoO_3 particles

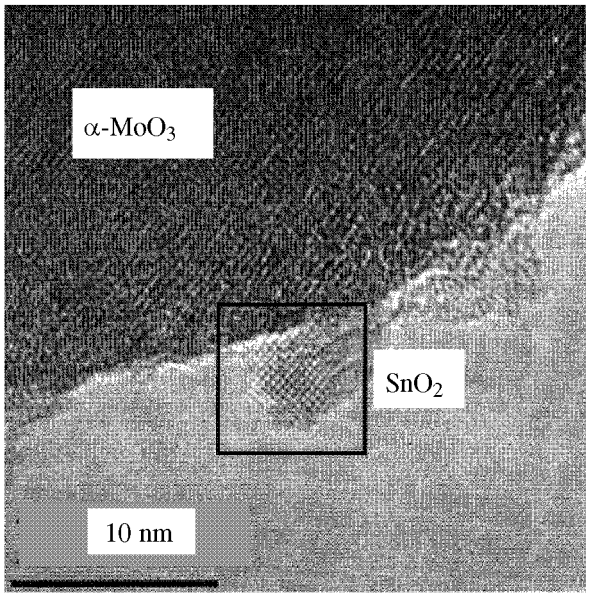

Fig. 4. High-resolution TEM image of SnO_2–MoO_3 ($x = 0.60$) nanocomposite.

is determined by the hybridized O 2*p*–Mo 4*d* orbitals [34] and corresponds to the octahedral surrounding of molybdenum with the orbital splitting in the crystal field into t_{2g} (M_1) and e_g (M_2) levels.

The distribution of molybdenum in the SnO_2–MoO_3 nanocomposites depends on the molybdenum content. At $0 \le x \le 0.12$, with increasing molybdenum content in the SnO_2 particles, the I_{S1}/I_{S2} ratio smoothly increases owing to an increase in the intensity of the S_1 line (535 eV). The Raman spectroscopic examination detects the β-MoO_3 phase at $x \ge 0.04$, which suggests a poor solubility of Mo(VI) in the cassiterite structure with most of Mo occurring on the SnO_2 crystallite surface as β-MoO_3 segregation.

In the $0.40 \le x \le 0.83$ range the surface of the tin dioxide particles gets saturated with molybdenum, which occurs in the nanocomposites predominantly as large α-MoO_3 particles.

The intermediate area ($0.17 \le x \le 0.26$) is characterized by a wide scatter of the data obtained in analysis of different nanoparticles, which suggests the β-MoO_3 → α-MoO_3 transition and reasonably agrees with the Raman spectroscopic and electron diffraction data.

Taken together, our experimental data suggest the following major relationships.

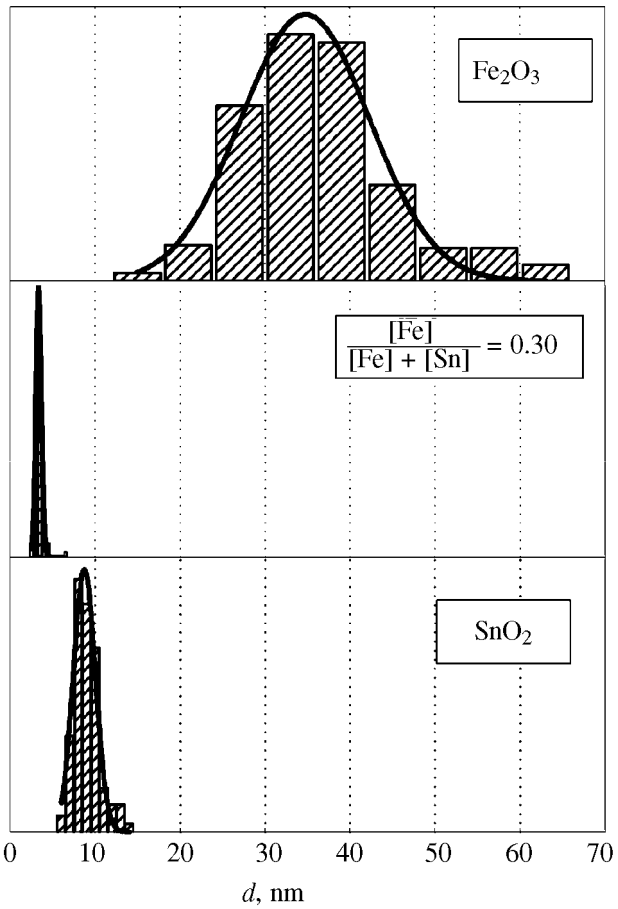

Fig. 5. Particle size distribution for SnO_2–Fe_2O_3 nanocomposites: annealing at 500°C.

(1) The synthesis method affects the mutual distribution of the components in the nanocomposites. When incorporated by impregnation, the second component is concentrated on the surface of the major phase crystallites. The diffusion rates in the solid phase are low, which kinetically hinders exhaustive incorporation of the second component into the crystal structure of the major phase. This facilitates crystallization of the oxide phase of the second component. The coprecipitation method affords a high degree of homogenization of the components, thereby increasing the probability of formation of solid solutions.

(2) With increasing content of the second component in the nanocomposites, a solid solution is consistently formed in the major component. Further, second component oxide segregates as a monolayer or islands on the surface of the major phase crystallites, followed by formation of a two-phase system.

(3) The size of the solid solution ranges depends on how close the ionic radii of M^{n+} and Sn^{4+} are and how defective, the SnO_2 structure. The distribution coefficient of the second component between the solid solution and the surface segregation cannot be precisely determined. With increasing annealing temperature, the SnO_2 structure gets less defective, and the solubility of the second component decreases.

(4) A high surface energy of the 3–5-nm SnO_2 particles in the SnO_2–MoO_3 nanocomposites is responsible for their stabilization as a surface segregation of the thermodynamically metastable β-MoO_3 phase.

PARTICLE SIZE AND SPECIFIC SURFACE AREA

The sensor signal and the catalytic activity of nanocrystalline oxides correlate with the specific surface area available for adsorption [35]. The specific surface area of the sensor materials is typically increased by decreasing the particle size. However, prolonged sensor measurements at elevated temperatures of 100–500°C result in aggregation of particles and a decrease in the stability of the sensor element.

The thermal stability of nanocrystalline materials is increased through modification of the crystal grain boundaries by the second component [36] or substitution of the surface hydroxy groups by other functional groups precluding particle condensation and aggregation [37]. Introduction of the second component causes decreases in both the total free energy at interfaces and the contact surface area of intrinsic crystallites for each of the ultradispersed phases. This considerably decelerates the crystal grain growth.

The transmission electron-microscopic examination showed that, with introduction of the second component, both the SnO_2 and Fe_2O_3 particles in the SnO_2–Fe_2O_3 nanocomposites decrease in size (Fig. 5) [13]. The average size of CSAs of SnO_2 and α-Fe_2O_3, estimated by the Scherer formula (2), suggests that, at all the annealing temperatures tested, the size of CSAs of the major phase decreases with introduction of the second component. Table 2 presents, for comparison, the CSAs of the major component phase (d_{SnO2}, d_{Fe2O3}), as well as the average particle size d_{ITEM} determined by transmission electron microscopy. A reasonable agreement of these data suggests that the average size of the crystal grains of the components in the

nanocomposites can be estimated from the broadening of the reflections in the X-ray diffraction patterns.

For all the nanocrystalline systems examined, the introduction of the second component causes the sizes of the major phase crystallites to decrease. The relative change of the crystal grain size d_{rel} is represented as

$$d_{rel} = \frac{d_0 - d}{d_0}, \quad (5)$$

where d is the size of the crystallites of the given phase in the nanocomposite, and d_0, size of the neat oxide crystallites at the same annealing temperature (Fig. 6). For example, the difference in the SnO_2 crystallite sizes is independent of the specific oxide (Fe_2O_3, MoO_3, or V_2O_5) introduced as the second component of the nanocomposite. The crystallite size difference d_{rel} tends to increase as $V_2O_5 \approx MoO_3 < Fe_2O_3 < SnO_2$. This tendency correlates with the growth of the Tamman temperature ($0.5T_{melt}$) of these oxides:

V_2O_5 (482 K) < MoO_3 (534 K) < Fe_2O_3 (919 K) < SnO_2 (1136 K)

Thus, the lower the mobility of the crystal lattice ions in the major phase of the nanocomposite, the stronger the influence exerted by the second component on the growth rate of the crystal grains of the matrix.

The specific surface area S_{sp} of the nanocomposites is determined by the mode of introduction of the second component and annealing temperature [13–16]. In all cases, certain areas can be identified on the plot of S_{sp} vs. the composition (Fig. 7). The single-phase area from the SnO_2 side is characterized by high S_{sp} values and an increase in the surface area with increasing x owing to a decrease in the SnO_2 particle size. At a low annealing temperature T = 300°C, impregnation of tin dioxide with a large amount of the precursor of the second component results in formation of large particles of the second phase and a decrease in S_{sp} relative to SnO_2. The single-phase area from the $M^{II}O$ side is characterized by low S_{sp} values, which is consistent with a large size of the $M^{II}O$ particles. The two-phase area corresponds to intermediate S_{sp} values; the specific surface area decreases with increasing x because of increases in the proportion and size of the $M^{II}O$ particles.

SENSOR PROPERTIES OF THE NANOCOMPOSITES

We analyze below the sensor properties of the SnO_2–Fe_2O_3, SnO_2–V_2O_5, and SnO_2–MoO_3 nanocomposites. As tested gases we chose NH_3, a typical Lewis base, and C_2H_5OH, whose molecule comprises donor and acceptor groups [14, 16, 30, 38, 39].

Table 2. Size of the CSAs for the major component in the SnO_2–Fe_2O_3 nanocomposites and particle sizes determined by TEM

$x = \frac{[Fe]}{[Fe] + [Sn]}$	X-ray diffraction		TEM
	d_{SnO2}, nm	d_{Fe2O3}, nm	d_{TEM}, nm
0.00	9	—	9 ± 1
0.03	7	—	6.2 ± 0.6
0.08	6	—	4.4 ± 0.6
0.13	5	—	5.5 ± 0.7
0.31	4	—	3.4 ± 0.3
0.37	< 3	< 3	4.3 ± 0.7
0.52	—	8	8 ± 5
0.69	—	11	14 ± 3
0.85	—	10	33 ± 7
1.00	—	24	35 ± 8

NH_3 Detection

Table 3 presents the sensor responses from nanocomposites to NH_3. In the SnO_2–MoO_3 and SnO_2–

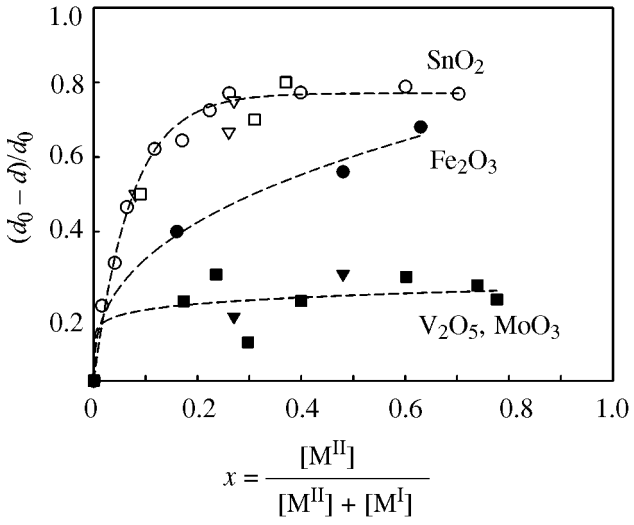

Fig. 6. Relative change of the size of the major phase crystallites vs. second component proportion in the nanocomposites annealed at 500°C.

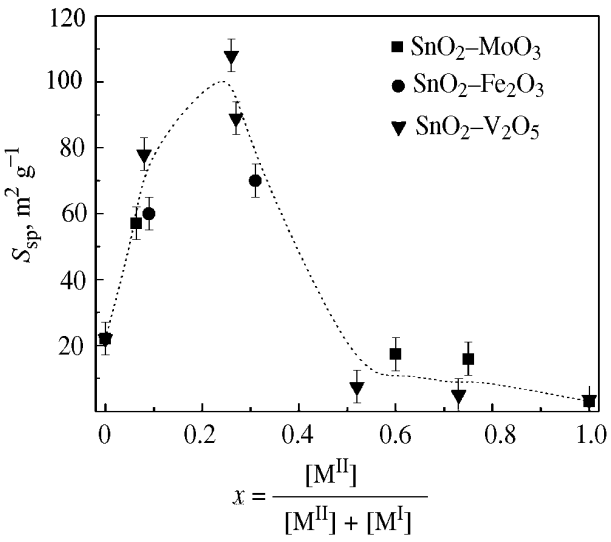

Fig. 7. Specific surface area vs. the composition of the nanocomposites: annealing at 500°C.

V_2O_5 systems, $S(NH_3)$ passes through a maximum with increasing x. The maximal S values correspond to the $0.25 < x < 0.55$ composition range. For SnO_2–Fe_2O_3 nanocomposites, the sensor response monotonically decreases with increasing iron content.

To compare the acid properties of the nanocomposites [38, 39] and their sensitivities to ammonia, we estimated the number of the centers per squared meter of the sample surface, for which the ammonia desorption activation energy is 130–150 kJ mol^{-1}, which corresponds to the optimal, for ammonia detection, temperature range 300–500°C. We calculated the distribution of the adsorption centers with respect to the ammonia desorption activation energy in terms of the model presented in [40].

Table 3. Sensor response from nanocomposites to ammonia $S(NH_3)$

SnO_2–Fe_2O_3		SnO_2–MoO_3		SnO_2–V_2O_5	
x	$S(NH_3)$	x	$S(NH_3)$	x	$S(NH_3)$
0.00	2.7 ± 0.3	0.00	1.5 ± 0.2	0.00	3.2 ± 0.3
0.08	2.5 ± 0.2	0.05	3.5 ± 0.3	0.13	4.1 ± 0.4
0.84	0.7 ± 0.2	0.17	4.8 ± 0.5	0.52	6.7 ± 0.5
1.00	0.5 ± 0.1	0.22	6.5 ± 0.5	1.00	1.7 ± 0.2
		0.40	7.0 ± 0.5		
		0.50	6.0 ± 0.5		
		0.70	5.0 ± 0.5		
		1.00	2.5 ± 0.2		

For all the systems examined, the sensor response monotonically increases with increasing number of the corresponding acid centers (Fig. 8). Thus, chemisorption of ammonia on the Lewis acid centers with charge transfer from the NH_3 molecule to the oxide surface [41] is the major factor responsible for the change in the conductivity.

C_2H_5OH Detection

In the reaction with ethanol vapor, the SnO_2–Fe_2O_3 nanocomposites exhibit identical trends in variation of the number of the acid centers and the sensor response with the composition of the sample. The SnO_2–V_2O_5 and SnO_2–MoO_3 systems exhibit opposite trends: With increasing x, the increase in the total acidity is accompanied by a decrease in the sensor response to ethanol (Table 4) [14, 30, 38].

The size of the sensor signal depends both on the number of adsorption centers on the sample surface and on their nature. There exist two major mechanisms of ethanol conversion [42]: dehydration and oxidative dehydrogenation. The first mechanism operates predominantly on the surface containing Brønsted acid centers, and results in a low sensor response. By contrast, the dehydration mechanism is realized with pairs of Lewis acid and base centers [43]. This interaction type implies a change in the electric conductivity of the material owing to the reaction with the chemisorbed oxygen O_s^-:

$$C_2H_5OH + O_s^- \rightarrow CH_3CHO + H_2O + e^-. \quad (6)$$

On the surface of the metal oxide-based nanocomposites, the coordination-unsaturated metal cations

Table 4. Sensor response from nanocomposites to ethanol $S(C_2H_5OH)$

SnO_2–Fe_2O_3		SnO_2–MoO_3		SnO_2–V_2O_5	
x	$S(C_2H_5OH)$	x	$S(C_2H_5OH)$	x	$S(C_2H_5OH)$
0.00	15.2 ± 0.3	0.00	20.5 ± 0.8	0.00	19.2 ± 0.5
0.08	17.3 ± 0.5	0.05	12.3 ± 0.5	0.13	5.7 ± 0.4
0.84	17.1 ± 0.5	0.50	6.1 ± 0.5	0.52	4.2 ± 0.5
1.00	6.2 ±0.3	0.70	5.5 ± 0.5	1.00	2.1 ± 0.2
		1.00	4.0 ± 0.5		

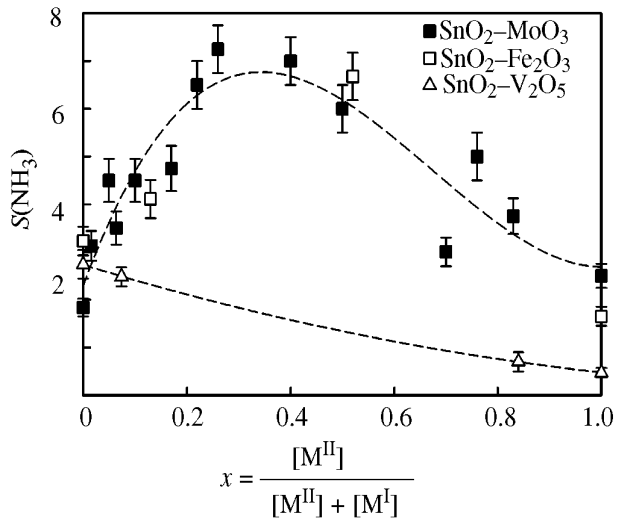

Fig. 8. Sensor response from nanocomposites to NH_3 vs. the number of the corresponding acid centers.

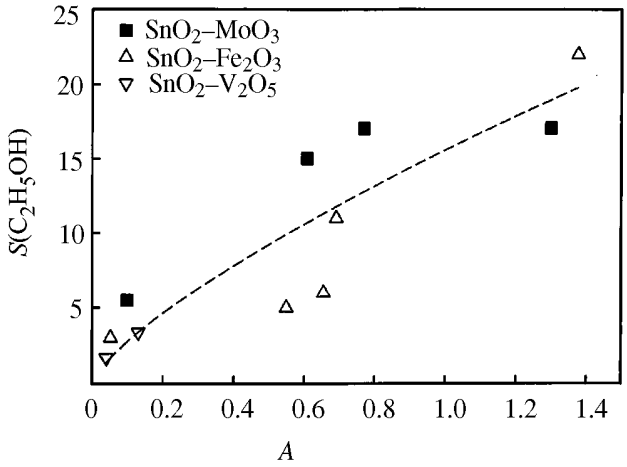

Fig. 9. Sensor response from nanocomposites to ethanol vs. the ratio of the numbers of Lewis to Brønsted acid centers.

and chemisorbed oxygen particles act as the Lewis acid and base centers, respectively. At identical adsorption powers of the samples, the selectivity of the ethanol conversion to acetaldehyde and the sensor response depend on the ratio of the number of strong (Lewis) to weak (Brønsted) acid centers. On the surface containing Brønsted centers, ethanol is dehydrated to C_2H_4; such materials are weakly sensitive to alcohols. The samples dominated by Lewis centers, on the contrary, exhibit a strong response to C_2H_5OH owing to dehydrogenation.

The Brønsted (A_{weak}) and Lewis (A_{strong}) acidities of the nanocomposites can be characterized by the surface concentration of the acid centers from which ammonia is desorbed at temperatures within 25–200°C and 350–600°C, respectively. For all the series of the nanocomposites, the sensor response to ethanol correlates with the ratio between the Lewis and Brønsted surface acidities A_{strong}/A_{weak} (Fig. 9).

CONCLUSION

We revealed certain correlations between the chemical features of the surface and the sensor properties of nanocrystalline oxide-based materials. Surface modification of semiconductor oxides with catalysts allows controlling the type and density of the acid centers and redox properties of the surface, thereby increasing the selectivity of materials.

The mutual distribution of the components between the surface and bulk of the crystallites in $M^{I}O$–$M^{II}O$ nanocrystalline systems has a complex nature. We showed that the ranges of existence of solid solutions and the phase formation conditions in such systems are strongly affected by their particle size distribution.

Considering a small size of the particles, mutually complementing methods should be used to characterize the nanocrystalline systems: Along with X-ray diffraction, important information on the structure of such systems can be derived from scanning electron microscopic, electron diffraction, and Raman and Mössbauer spectroscopic examinations.

ACKNOWLEDGMENTS

This study was carried out in cooperation with the University of Barcelona (Spain), University of Brecia (Italy), and the Laboratory of Kinetics and Catalysis, Chemical Department, Lomonosov Moscow State University, and was financially supported by the Government of France (in the framework of the agreement between the Institut National Polytechnique de Grenoble and Lomonosov Moscow State University on joint supervision of post-graduate students' work), INTAS (project nos. 93-0091 and 2000-0066), the "Science for Peace" NATO program (project no. CBP.NR.NRSFP 982166), the International Scientific and Technical Center (project ISTC#3424), Russian

Foundation for Basic Research (RFBR)-PICS program (project no. RFBR 98-03-2207–PICS-592), and Russian Foundation for Basic Research?RFBR (project nos. 06-03-32395 and 06-03-39001).

REFERENCES

1. Yamazoe, N., *Sens. Actuat. B*, 2005, vol. 108, p. 2.
2. Gopel, W. and Schierbaum, K.D., *Sens. Actuat. B*, 1995, vols. 26–27, p. 1.
3. Barsan, N., Schweizer-Berberich, M., and Gopel, W., *Fresenius J. Anal. Chem*., 1999, vol. 365, p. 287.
4. Takahata, K., in: *Chemical Sensor Technology,* Seiyama, T., Ed., Amsterdam: Elsevier, 1988, p. 39.
5. Souteyrand, E., in: *Les capteurs chimiques*, Pijolat, C., Ed., Lyon: CMC2, Ecole Centrale, 1997, p. 52.
6. Vol'kenshtein, F.F., *Elektronnaya teoriya kataliza na poluprovodnikakh* (Electronic Theory of Catalysis on Semiconductors), Moscow: Fizmatgiz, 1960.
7. Idriss, H. and Barteau, M.A., *Adv. Catal*., 2000, vol. 45, p. 261.
8. Cimino, A. and Stone, F.S., *Adv. Catal*., 2002, vol. 47, p. 141.
9. Freund, H.-J., Bäumer, M., and Kuhlenbeck, H., *Adv. Catal*., 2000, vol. 45, p. 333.
10. Kudryavtseva, S.M., Vertegel, A.A., Kalinin, S.V., et al., *J. Mater. Chem*., 1997, vol. 7, p. 2269.
11. Safonova, O., Bezverkhy, I., Fabritchny P., et al., *J. Mater. Chem*., 2002, vol. 12, p. 1174.
12. Rumyantseva, M.N., Safonova, O.V., Bulova, M.N., et al., *Izv. Ross. Akad. Nauk, Ser. Khim.*, 2003, vol. 52, no. 6, p. 1151.
13. Rumyantseva, M.N., Kovalenko, V.V., Gaskov, A.M., et al., *Sens. Actuat. B*, 2005, vol. 109, no. 1, p. 64.
14. Makeeva, E.A., Rumyantseva, M.N., and Gas'kov, A.M., *Neorg. Mater*., 2005, vol. 41, no. 4, p. 442.
15. Rumyantseva, M.N., Gaskov, A.M., Rosman, N., et al., *Chem. Mater*., 2005, vol. 17, no. 4, p. 893.
16. Kovalenko, V.V., *Cand. Sci. (Chem.) Dissertation*, Moscow, 2006.
17. Shannon, R.D. and Prewitt, C.T., *Acta Cryst. B*, 1969, vol. 25, p. 925.
18. Fabrichnyi, P.B., Babeshkin, A.M., Nesmeyanov, A.N., and Onuchak, V.N., *Fiz. Tverd. Tela*, 1970, vol. 12, no. 7, p. 2032.
19. Kovalenko, V.V., Rumyantseva, M.N., Fabritchnyi, P.B., and Gaskov, A.M., *Mendeleev Commun*., 2004, vol. 14, no. 4, p. 140.
20. Abello, L., Bochu, B., Gaskov, A., et al., *J. Solid State Chem*., 1998, vol. 135, p. 78.
21. Boulova, M., Galerie, A., Gaskov, A., and Lucazeau, G., *Sens. Actuat. B*, 2000, vol. 71, p. 134.
22. Kündig, W., Bömmel, H., Constabaris, G., and Lindquist, R.H., *Phys. Rev.*, 1966, vol. 142, p. 327.
23. Fabritchnyi, P.B., Babeshkin, A.M., and Nesmeianov, A.N., *J. Phys. Chem. Solids*, 1971, vol. 32, p. 1701.
24. Fabritchnyi, P.B., Lamykin, E.V., Babeshkin, A.M., and Nesmeianov, A.N., *Solid State Commun*., 1972, vol. 11, p. 343.
25. Berentsveig, V.V., Hasan, Z.A., Fabritchnyi, P.B., et al., *React. Kinet. Catal. Lett.*, 1980, vol. 15, p. 239.
26. Khramov, D.A. and Urusov, V.S., *Neorg. Mater*., 1983, vol. 19, no. 11, p. 1880.
27. Ichiba, S. and Yamaguchi, T., *Chem. Lett*., 1984, vol. 13, no. 10, p. 1681.
28. Schneider, F., Melzer, K., Mehner, H., and Dehe, G., *Phys. Stat. Sol. A*, 1977, vol. 39, no. 2, p. K115.
29. Berry, F.J., Greaves, C., McManus, J.G., et al., *J. Solid State Chem*., 1997, vol. 130, no. 2, p. 272.
30. Arbiol, J., Morante, J.R., Bouvier, P., et al., *Sens. Actuat. B*, 2006, vol. 118, p. 156.
31. Harb, F., Gerand, B., Nowogrocki, G., and Figlarz, M., *Solid State Ionics*, 1989, vols. 32–33, p. 84.
32. Moreno, M.S., Egerton, R.F., and Midgley, P.A., *Phys. Rev. B*, 2004, vol. 69, p. 233304/1.
33. Moreno, M.S., Egerton, R.F., Rehr, J.J., and Midgley, P.A., *Phys. Rev. B*, 2005, vol. 71, p. 035103/1.
34. Wang, D., Su, D.S., and Schlögl, R., *Z. Anorg. Allg. Chem*., 2004, vol. 630, p. 1007.
35. Li, G.-J., Zhang, X.-H., and Kawi, S., *Sens. Actuat. B*, 1999, vol. 60, p. 64.
36. Gleiter, H., *Acta Mater*., 2000, vol. 48, p. 1.
37. Wu, N.L., Wang, S.-Y., and Rusakova, I.A., *Science,* 1999, vol. 285, p. 1375.
38. Rumyantseva, M., Kovalenko, V., Gaskov, A., et al., *Sens. Actuat. B*, 2006, vol. 118, p. 208.
39. Kovalenko, V.V., Zhukova, A.A., Rumyantseva, M.N., et al., *Sens. Actuators B*, 2007, vol. 126, p. 52.
40. Yushchenko, V.V., *Zh. Fiz. Khim*., 1997, vol. 71, p. 628.
41. Abee, M.W. and Cox, D.F., *Surf. Science*, 2002, vol. 520, p. 65.
42. Jinkawa, T., Sakai, G., Tamaki, J., et al., *J. Mol. Catal. A*, 2000, vol. 155, p. 193.
43. Idriss, H. and Seebauer, E.G., *J. Mol. Catal. A*, 2000, vol. 152, p. 201.